Petroleum Science 23 (2026) 1505–1518

Contents lists available at ScienceDirect

Petroleum Science

journal homepage: www.keaipublishing.com/en/journals/petroleum-science

Original Paper

A cascaded pipeline defect detection and size estimation method based on the YOLOv11 and physics-informed network using the MFL data

Xi-Ming Chen, Meng-Kai Fu, Jia Shao, Xiao-Ben Liu *

National Engineering Research Center for Pipeline Safety/MOE Key Laboratory of Petroleum Engineering/Beijing Key Laboratory of Urban Oil and Gas Distribution Technology, China University of Petroleum (Beijing), Beijing, 102249, China

ARTICLE INFO

Article history:
Received 6 May 2025
Received in revised form
6 August 2025
Accepted 6 August 2025
Available online 9 August 2025

Edited by Jia-Jia Fei

Keywords:
Oil and gas pipeline
MFL inspection
Defect detection
Defect size estimation

ABSTRACT

Long-distance oil and gas pipelines are crucial in the global energy network. However, due to complex internal and external environments, defects can be formed on a pipeline's surface, posing severe threats to structural safety. Aiming to detect surface defects, recent works have used magnetic flux leakage (MFL) inspection data for defect recognition and defect size estimation. Accurately locating and measuring defects based on the MFL data is essential for pipeline integrity assessment and safety maintenance. To obtain effective MFL data on pipeline defects, this study constructs an experimental pipeline at the Daxing pulling-through test site in Beijing. An ultra-high-definition MFL inspection robot is employed to collect defect data, which are then used to construct a defect detection and size estimation database. In addition, to achieve precise defect recognition and quantification, a cascaded method, which integrates a mature computer vision detection model, the YOLOv11 model, with a physics-informed and data-driven prior deep-learning quantification model, is proposed. Validation results show that, even for a limited amount of data, the proposed defect recognition model can achieve an AP50 of 92.1% at a confidence threshold of 0.6, a precision of 100%, a recall of 84.29%, and an F1-score of 91.47 %, indicating high accuracy in identifying surface defects on pipelines. The quantification model can achieve the goodness of fit (Gof) values of 0.987, 0.979, and 0.994 for defect length, width, and depth, with the mean absolute percentage error (MAPE) of 7.97%, 8.52%, and 4.74%, respectively. Comparison analysis with different models confirms the superiority of the proposed cascaded recognition and quantification approach. The results also demonstrate that the proposed method can effectively identify and quantify defects in long-distance pipelines. Finally, it can improve the interpretation efficiency of MFL inspection data and provide reliable support for residual strength assessment and remaining life prediction of pipelines.

1. Introduction

With the continuous increase in the global energy demand, the importance of oil and gas pipelines in the global energy network has increased significantly. The safe operation of pipelines, which denote the backbone of national economies, directly impacts public welfare, economic stability, and global industrial development (Kim et al., 2018). Although pipelines are considered the safest and most reliable method for long-distance transportation of oil and gas resources, they can suffer serious damage yearly due to various defects, such as corrosion, metal loss, and illegal tapping (Long et al., 2021; Zarifi et al., 2018), which can further lead to substantial economic losses and even casualties (Chen et al., 2021; Xie and Tian, 2018). According to statistics from the U.S. Pipeline and Hazardous Materials Safety Administration (PHMSA), over 700 pipeline leakage incidents have been reported, where corrosion-related failures accounted for 22.39% (Cole and Marney, 2012), causing direct and indirect economic losses of hundreds of millions of dollars (Liu and Bao, 2022; Peng et al., 2020). Therefore, regular pipeline integrity

* Corresponding author.
E-mail address: xiaobenliu@cup.edu.cn (X.-B. Liu).
Peer review under the responsibility of China University of Petroleum (Beijing).

https://doi.org/10.1016/j.petsci.2025.08.013

assessments are crucial for preventing accidents, mitigating environmental risks, avoiding casualties, and reducing economic losses (Parlak and Yavasoglu, 2023).

Among the existing pipeline integrity assessment methods, including hydrostatic testing (Ahmed et al., 2008), in-line inspection (ILI), and direct assessment of pipeline residual strength (Melo et al., 2020) methods, the ILI methods are the only methods that can provide information on pipeline geometric anomalies, load abnormalities, and material property deviations without compromising pipeline integrity. Various ILI methods have been applied to the industry, including the inertial navigation unit (INU)-based inspection method (Liu X.B. et al., 2021; Wang et al., 2023; Zhang D. et al., 2025), geometric inspection method, eddy current inspection method (Gao et al., 2014), ultrasonic inspection method (Reber et al., 2002), and magnetic flux leakage (MFL) inspection method. Among them, the MFL inspection method stands out for its excellent performance in detecting both internal and external pipeline defects. This method's performance is unaffected by a pipeline's transported medium and external environmental conditions and can provide highly accurate detection results. Consequently, the MFL method has gradually become the mainstream method for identifying structural defects in pipelines, offering critical support for pipeline structural integrity evaluations.

Early MFL inspection technology was primarily used to detect internal and external corrosion on pipeline walls, recording only the axial component of the leakage magnetic field. However, this made this technology relatively insensitive to axial defects, resulting in poor detection and identification performance for axial grooves and cracks (Feng et al., 2016; Liu et al., 2017). To satisfy the increasing requirements for higher detection rates and improved quantification accuracy, related literature has proposed three-axis ultra-high-resolution MFL technology. This advanced technology adds two sets of orthogonal Hall sensors to the traditional axial sensors, which allows for measuring circumferential and radial leakage magnetic signals. This can further ensure a more accurate and clearer representation of defect size characteristics (Miller and Sander, 2006).

To achieve accurate defect detection and identification using the MFL data, existing research has mainly employed data-driven approaches. Compared to traditional manual interpretation, data-driven methods have been widely studied due to their advantages of high efficiency, strong accuracy, and independence from physical theories and analytical modeling. Khodayari-Rostamabad et al. (2009) employed machine-learning algorithms to classify MFL inspection data, and the effectiveness of the proposed method was verified using experimental data. A research team from Northeastern University (China) developed a defect identification and classification method based on Random Forests (Liu et al., 2016); however, this method requires manual feature selection, making fully automated identification unfeasible. To address this limitation, the same team later used the Fast-RCNN model (Yu et al., 2023) and incorporated data augmentation techniques to realize intelligent defect detection based on the MFL data. Focusing on small defects, weld defects, and pipeline components, the team further developed a THMS-Net model (Jiang et al., 2022), a lightweight rotated network (Liu et al., 2024), and an MMB-Net (Zhao et al., 2024) to achieve high-precision detection of small pipeline defects, lightweight and accurate online detection of weld defects, and precise identification and classification of pipeline components using the MFL inspection data. To address the problem of data imbalance, Chen et al. (2024) designed a cascaded defect detection and classification approach, combining the You Only Look Once (YOLO) v5 and Vision Transformer models, which could effectively recognize and classify defects based on the MFL data.

Although the existing methods can accurately localize pipeline defects, obtaining precise defect dimensions remains the major challenge for full lifecycle pipeline integrity assessment. Deif and Daneshmand (2019) used a finite element-based discretization and numerical solving approach to calculate defect geometry iteratively, but their method struggled with solving complex problems. To improve the accuracy of defect size estimation, Long et al. (2022) and Zhang et al. (2023) respectively proposed the magnetic field spatial integration (MFSI) method and the discrete magnetic dipole model (DMDM) based on the magnetic dipole model, and validated the effectiveness of both methods through finite element simulations and laboratory test data. For instance, Sun et al. (2021) used pull-through MFL inspection datasets and data augmentation techniques to construct the DfedResNet model, which could achieve accurate fitting of defect dimensions. Zhang M. et al. (2022) developed a VDTL-based network model incorporating ADF and transfer learning techniques, and validated its effectiveness using both experimentally collected data and finite element simulation results. Yuksel et al. (2023) developed a defect quantification model based on the CR-CNN architecture and employed the SwinYOLOv5 model to extract images as inputs for the quantification model. Yuan et al. (2024) designed a defect MFL data augmentation method, combining different experimental and simulation approaches, and developed the ASTC-Net model for defect type classification and size quantification. Xu et al. (2024) established a sample database using pull-through testing and employed the AOA-XGBoost algorithm to quantify defect depth in pipelines accurately. The research team from Northeastern University (China) has developed several deep learning neural network models, such as MLKG-NN and EIC-Net, to accurately quantify the 3D dimensions of both regular and irregular defects (Wang et al., 2022, 2024, 2025). Building on this foundation, they further proposed a unified defect detection and quantification algorithm, TOPC-Net, which enables joint modeling of defect identification and size estimation based on MFL inspection data (Shen et al., 2025).

Although the existing studies have achieved accurate defect localization and size estimation using experimental data, several limitations remain. First, previous studies have generally relied on a large amount of labeled data, which is challenging to obtain in practical industrial applications. Second, the existing data-driven approaches for defect size quantification often overlook physical factors, resulting in poor model fitting performance and limited generalizability.

To address the aforementioned limitations, this study constructs a defect localization and size quantification database using the MFL inspection data obtained from pull-through testing. In addition, a pre-trained YOLOv11 model is used to develop a lightweight, high-precision defect localization model. Further, key features for defect size quantification are identified through the MFL mechanism analysis, and a physics-informed, data-driven prior deep-learning method is developed. This method enables accurate defect localization and size quantification based on small sample sizes.

2. Defect sample database construction

2.1. MFL inspection operational principles

The basic operational principle of the MFL ILI is to magnetize ferromagnetic materials to saturation using an external magnetic field, thus creating a strong magnetic field inside the material. When a pipeline is defect-free, the magnetic field lines are distributed parallel to the pipe, as shown in Fig. 1(a). However, when there are defects or pipe components, the magnetic field

distorts due to the low magnetic permeability and high magnetic resistance at a defect. Namely, the magnetic field lines change their path at a defect or pipe component and leak out of the structure. After crossing the defect or pipe component, they re-enter the material, creating a leakage magnetic field on the outside of the material (Yang, 2005), as illustrated in Fig. 1(b). This leakage magnetic field can be captured by Hall sensors and converted into electrical signals. Through further data processing and analysis, accurate defect localization and quantification can be achieved (Chen et al., 2021).

2.2. Pull-through testing

To obtain pipeline defect samples that reflect real-world conditions, this study used pull-through testing to construct a database. The steel pipeline used in the experiment was 103 m long and divided into 10 sections, which were connected by flanges or welds. The experiment was conducted at the PipeChina ull-through testing site in Daxing District, Beijing, China. During the test, defects were designed and processed based on the axial length, circumferential width, and relative depth. The designed defect sizes were 40 mm × 15 mm × 10%, 30 mm × 10 mm × 40%, 100 mm × 20 mm × 80%, and 25 mm × 60 mm × 20%, forming 134 sets of pipeline groove defects, both axial and circumferential, as illustrated in Fig. 2.

To ensure the validity of the measured data, improve data quality, and enhance the model's generalization ability (Han and Lang, 2023), defects were randomly distributed in the first four pipe sections, as shown in Fig. 3(a). This study used an triaxial ultra-high-definition (240-channel) MFL ILI robot for detection, as displayed in Fig. 3(b). Data were collected every 1.5° circumferentially, with one thousand data points per meter axially. The experimental pipeline had a diameter of 508 mm and a wall thickness of 7.9 mm. To reduce the sensor lift-off effect during the experiment, this study fixed the relative position of the MFL probe and moved the ILI robot along the pipeline's axis by an external winding engine at a speed of 0.5 m/s. During the inspection, the probe captured leakage magnetic flux signals using the Hall sensors; the collected signals were digitized by an analog-to-digital converter (ADC) and transmitted to the inspection system's storage device for subsequent offline analysis.

2.3. Data preprocessing

During the operation of the ILI robot, due to the complex characteristics inside the pipeline and variations among the Hall detection probes, the raw MFL data could contain baseline drift and high-frequency noise. To reduce the influence of noise and other factors on the defect detection and size estimation result, this study employed baseline correction and filtering methods to preprocess the MFL ILI data.

During the inspection process, differences in the baseline values of the Hall sensors mounted on the ILI robot could cause variations in the signal amplitudes at the same location across different sensors. Therefore, baseline calibration was performed on the original three-axis data to ensure consistent baseline levels across all sensors. This improved the validity of the inspection data and reduced defect detection and size estimation errors caused by baseline differences (Shen et al., 2023; Yu et al., 2023). The baseline calibration formula was defined as follows:

$$H^{*}_{i,j} = H_{i,j} - \frac{1}{n}\sum_{i=1}^{n} H_{i,j} + \frac{1}{nm}\sum_{j=1}^{m}\sum_{i=1}^{n} H_{i,j}, \tag{1}$$

where $H^{*}_{i,j}$ represents the MFL signal at position (i,j) after baseline calibration; $H_{i,j}$ is the MFL signal at position (i, j) before baseline calibration; n is the number of sampling points per channel; m is the number of MFL signal channels.

To reduce the impact of high-frequency noise on the developed model's performance, this study applied a two-dimensional Gaussian filter to the calibrated data. This filtering process attenuated high-frequency noise, denoising the MFL ILI data.

$$H^{\mathrm{Deno}}_{i,j} = G(x)\cdot H^{*}_{i,j}, \tag{2}$$

where $G(x)$ is the Gaussian filtering function, and $H^{\mathrm{Deno}}_{i,j}$ is the MFL ILI signal after filtering.

The MFL data, after baseline calibration and Gaussian filtering, could effectively reduce the impact of baseline variation and high-frequency noise on the defect detection performance, thus enhancing the defect features of the MFL signals, as shown in Fig. 4.

2.4. Pipeline defect database construction

After data preprocessing, aiming to construct the MFL data target detection database and being inspired by the research (Liu et al., 2024; Zhao and Tian, 2024) and other research results, this study demonstrates that pseudo-color images perform better because they retain more original MFL signal details (Ren et al., 2024), which enhances the robustness of defect location identification. By intuitively presenting signal intensity and distribution patterns on a plane through color gradients, this approach significantly improves data readability and representational capability. However, curve graphs, due to the presence of large blank areas and lack of continuous interpolation, have poor data

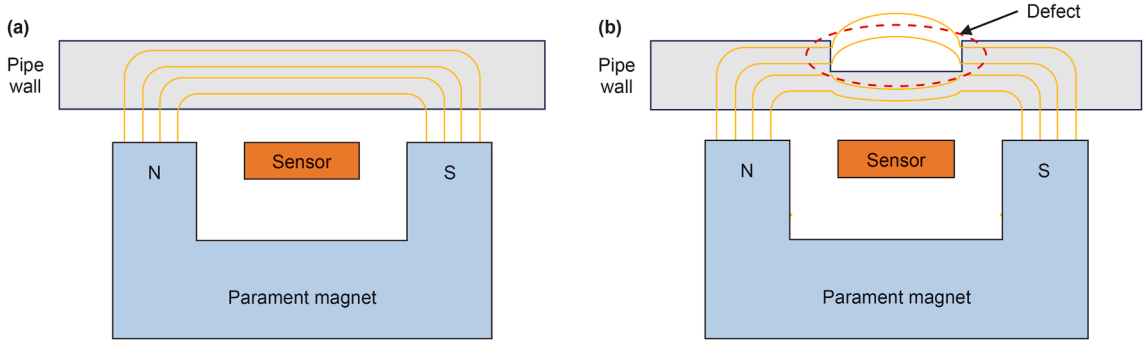

Fig. 1. The MFL inspection principle and magnetic field distribution: (**a**) magnetic field distribution on a defect-free pipe wall; (**b**) magnetic field distribution on a pipe wall with a defect.

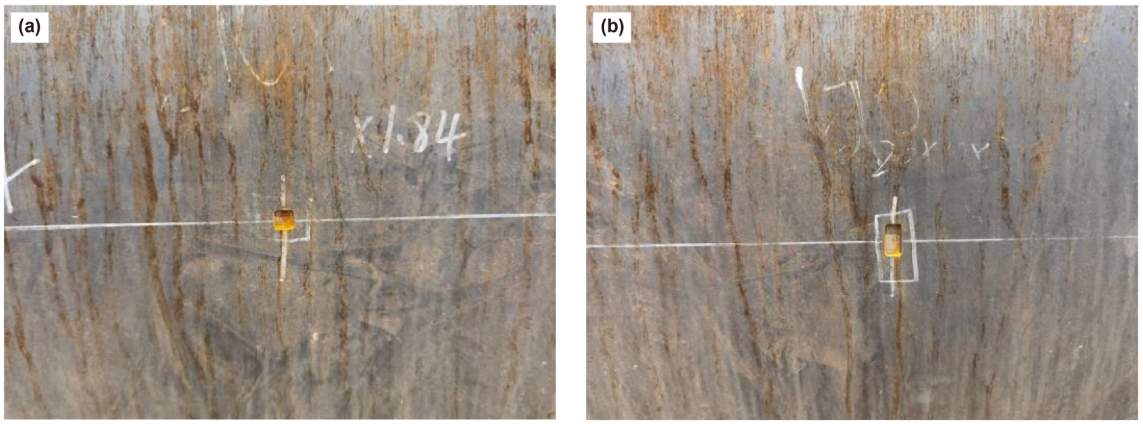

Fig. 2. Pull-through testing of the designed defects: (**a**) defect a; (**b**) defect b.

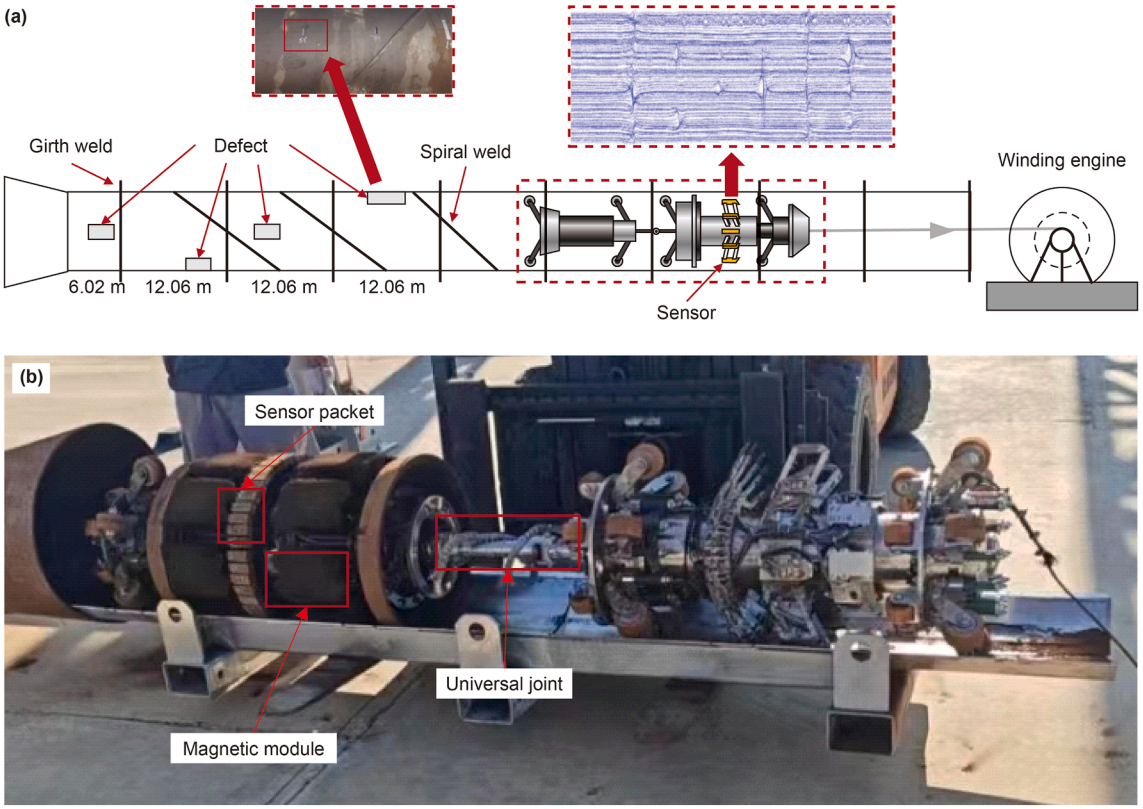

Fig. 3. The pull-through testing process: (**a**) pull-through testing procedure; (**b**) MFL ILI robot.

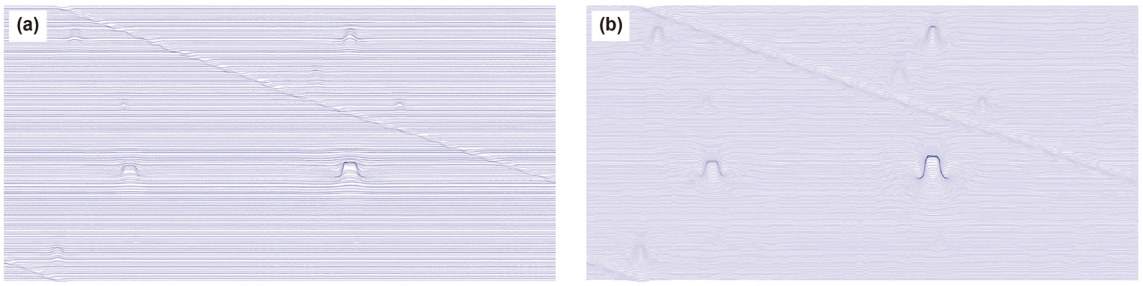

Fig. 4. Effectiveness of data preprocessing: (**a**) original data; (**b**) preprocessed data.

representation ability (Guo et al., 2024), limiting the generalization ability of the detection model. The preprocessed axial (y-axis) MFL single-channel data are mapped into a three-channel pseudo-color image. To ensure that each preprocessed axial MFL signal point $H_{i,j}^{\mathrm{Deno}}$ lies within the pixel range of [0, 255], a mapping transformation is applied to each point. The specific transformation method is expressed as follows:

$$G_{i,j} = \frac{255\left(H_{i,j}^{\mathrm{Deno}} - H_{i,j_{\min}}^{\mathrm{Deno}}\right)}{H_{i,j_{\max}}^{\mathrm{Deno}} - H_{i,j_{\min}}^{\mathrm{Deno}}}, \tag{3}$$

where $H_{i,j_{\max}}^{\mathrm{Deno}}$ is the maximum value of the preprocessed y-axis MFL data, $H_{i,j_{\min}}^{\mathrm{Deno}}$ is the minimum value of the preprocessed y-axis MFL data, and $G_{i,j}$ is the mapped signal value, as shown in Fig. 5. In the pseudo-color representation of MFL inspection data, the Gaussian value exhibits a positive correlation with pixel brightness: as the Gaussian value increases, the corresponding pixel becomes brighter; conversely, lower Gaussian values result in darker pixels.

To obtain the ground truth (GT) for pipeline defect location data, this study uses X-AnyLabeling to annotate the x and y coordinates of the bounding box center, as well as the width and height of the bounding box of the target defect within the pseudo-color image. These annotations are then normalized to construct the GT labels, as illustrated in Fig. 6.

The preprocessed MFL data are used to extract triaxial defect samples along the x-, y-, and z-axis based on the pipeline defect blueprint, as shown in Fig. 7(a–c), respectively. The center coordinates of each defect (including mileage and channel position) are obtained based on the defect blueprint, and corresponding defect samples are extracted. The extraction range spans 0.1 m before and after the mileage position, and 20 channels to the left and right of the central channel. The resulting MFL data samples have a size of 3 × 200 × 40. The defect sample size labels are constructed according to the defect blueprint. After screening, a total of 134 valid defect size samples are created.

3. Cascaded defect detection and size estimation model

To accurately recognize defect locations and quantify defect sizes from the MFL data acquired by the ILI robot, this study proposes a cascaded deep-learning method. This method combines the pre-trained YOLOv11 defect detector with a physics-informed, data-driven prior deep-learning model estimator. In addition, due to the small number of model parameters, the training process of the detector model is fast and efficient, providing an effective method for pipeline integrity assessment (PIA) through a small number of offline MFL data analyses. The research conducted in this study focuses on providing a general solution to the detection and size estimation of common pipeline defects, such as grooves and uniform corrosion.

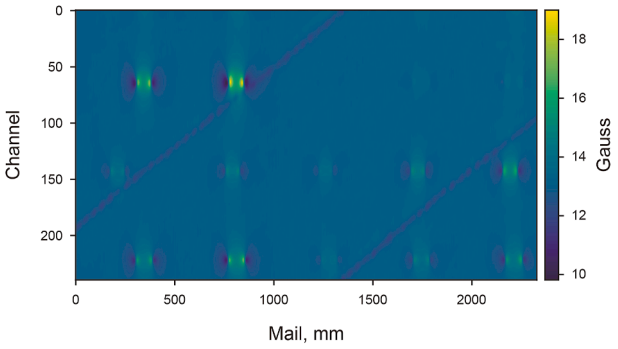

Fig. 5. The pseudo-color image of the MFL data (y-axis).

3.1. Defect detection model

To achieve accurate defect recognition in pipelines, this study employs the latest generation YOLOv11 object detection algorithm developed by Ultralytics, which is shown in Fig. 8. This algorithm has significantly improved recognition accuracy, speed, and computational efficiency compared to the previous algorithms. Similar to the other YOLO algorithms (Akdoğan et al., 2025; Nepal and Eslamiat, 2022; Redmon et al., 2016), the YOLOv11 algorithm is mainly composed of four parts: an input block, a backbone network, a neck network, and a detection head. Compared to the YOLOv8 model, the YOLOv11 model primarily improves the backbone and neck network architecture by replacing the C2F layer of the YOLOv8 model (Zhang Z. et al., 2025) with a C3K2 layer and introducing variable convolution kernels (multi-scale convolution) and a channel separation strategy. This enhances the model's receptive field and improves its ability to capture contextual information. In addition, the YOLOv11 model integrates the cross-stage partial (CSP) (Wang et al., 2020) structure and the pyramid squeeze attention (PSA) (Zhang H. et al., 2022) mechanism, which improves the model's ability to extract multi-scale features, allowing for effective capturing of defect features of different sizes. To reduce the number of parameters, the YOLOv11 model introduces depthwise convolution (Howard et al., 2017) into the detection head, which independently performs spatial convolutions on each channel of the input feature map, thus effectively reducing the model's parameter number. Compared to the traditional convolution types, depthwise convolution reduces the parameter numbers by $(1/C_{\mathrm{out}} + 1/K^2)$; this can effectively reduce the computational complexity and parameter number of the model while maintaining its performance. In addition, to ensure the model's effectiveness for small sample sizes, this study uses the pre-trained YOLOv11n model released by Ultralytics.

3.2. Physics-informed and data-driven prior deep-learning model for defect size estimation

3.2.1. Defect physical features selection

To integrate the physical information features of MFL ILI data into the deep-learning network, this study analyzes the features of these data using the MFL magnetic dipole model (Liu B. et al., 2021). Taking the defect center as the origin, the circumferential, axial, and radial directions of the pipeline are defined as the x-, y-, and z-axis, respectively. For each magnetic charge element $\mathrm{d}p = \sigma_s \mathrm{d}x\mathrm{d}z$, the corresponding magnetic field $\mathrm{d}\boldsymbol{H}$ at a distance r is calculated as follows:

$$\mathrm{d}\boldsymbol{H} = \frac{\mathrm{d}p}{4\pi r^3}\cdot r, \tag{4}$$

where σ_s is the pipe surface's magnetic charge density.

When the pipeline ILI device moves along the axial direction of the pipeline, the magnetic field intensity at the MFL inspection probe's location can be obtained by integrating Eq. (4), which yields:

$$\boldsymbol{H}(x,y,z) = \iint \mathrm{d}\boldsymbol{H} = \iint \frac{\mathrm{d}p}{4\pi r^3}\cdot r. \tag{5}$$

Based on Eq. (5) and considering the MFL inspection signal

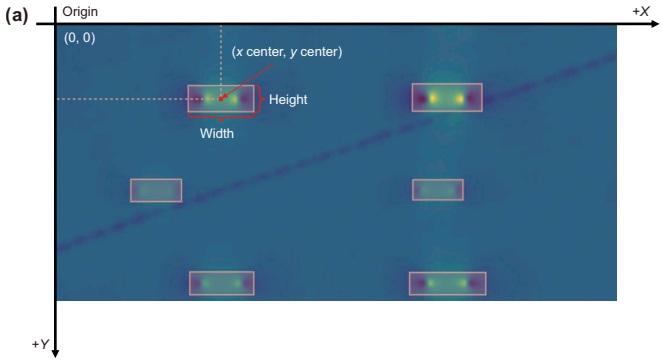

(b)

Defect	x center	y center	Width	Height
0	0.299886	0.270388	0.142367	0.131207
0	0.182390	0.598405	0.106346	0.110490
0	0.300743	0.922969	0.140652	0.103584
0	0.697827	0.270388	0.142367	0.145018
0	0.684105	0.588047	0.118353	0.089773
0	0.702115	0.922969	0.140652	0.110490

Fig. 6. Defect detection dataset labeling: (**a**) image; (**b**) label.

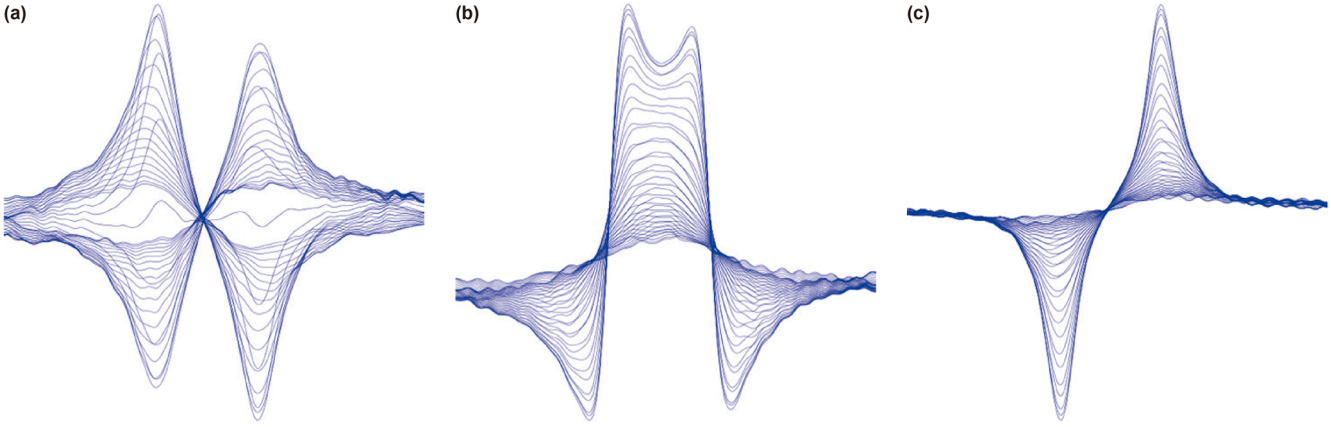

Fig. 7. Defect sample: (**a**) *x*-axis; (**b**) *y*-axis; (**c**) *z*-axis.

characteristics of defects with various sizes, the following analysis can be conducted.

1) The extrema of the H_x signal correspond to the circumferential edges of the pipeline defect, so the defect's circumferential width can be determined using the peak and valley values of the circumferential MFL signal.
2) The H_y signal's variations are mainly concentrated at the axial edges of the pipeline defect, making it suitable for determining its axial length. In addition, as the defect depth increases, the peak value of the H_y signal also increases. Therefore, both the peak-to-valley value of the axial signal and the waveform area of the axial signal are considered to be related to the pipeline defect's depth.
3) The H_z signal exhibits a peak and a valley on each side of the defect, making this feature suitable for determining the depth's defect.

In this study, as shown in Table 1, six physical information features are selected, and a representative feature set [f_1, f_2, f_3, f_4, f_5, f_6] is constructed to constrain the feature search space during model training based on physical prior knowledge. These features have clear physical correspondences with the geometrical parameters of pipeline defects, including circumferential width, axial length, and depth, and are therefore referred to as physically meaningful features.

3.2.2. Defect size estimation model

To achieve accurate fitting and extraction of defect geometric features based on three-dimensional MFL ILI data, this study uses a convolutional neural network (CNN) to construct the feature extraction layer. The CNN model, as a deep neural network architecture, stacks multiple convolutional modules to optimize feature parameters while automatically extracting the key features from the input data (Zhang et al., 2021; Zhao et al., 2021). This avoids the reliance on feature engineering common in traditional methods. The core mechanism of the CNN model is based on the gradient descent method, which is employed to find the global optimal solution, and a backpropagation method, which is used to adjust neuron weights dynamically. The model's prediction accuracy is continuously improved through multiple rounds of iterative training.

The CNN model used in this study combines convolutional layers, batch normalization layers, ReLU activation function layers, and max-pooling layers to create a hierarchical feature extraction module. In addition, convolution operations are introduced to extract local feature patterns; batch normalization improves the model's training stability; ReLU activation enhances the nonlinear expression of features; finally, max-pooling is selected for dimensionality reduction and feature invariance enhancement. In addition, to prevent model overfitting, dropout layers are added to some of the convolution blocks. The proposed model uses the progressive stacking of multi-layer convolutional modules to capture deeper, higher-dimensional features and adopts fully connected layers to regress the extracted features, ultimately producing the output defect geometric dimensions. The structural parameters of the CNN deep-learning model are shown in Table 2.

This study uses physical information features to constrain the model's search space and enhance the model's physical interpretability and generalization ability. Further, the geometric

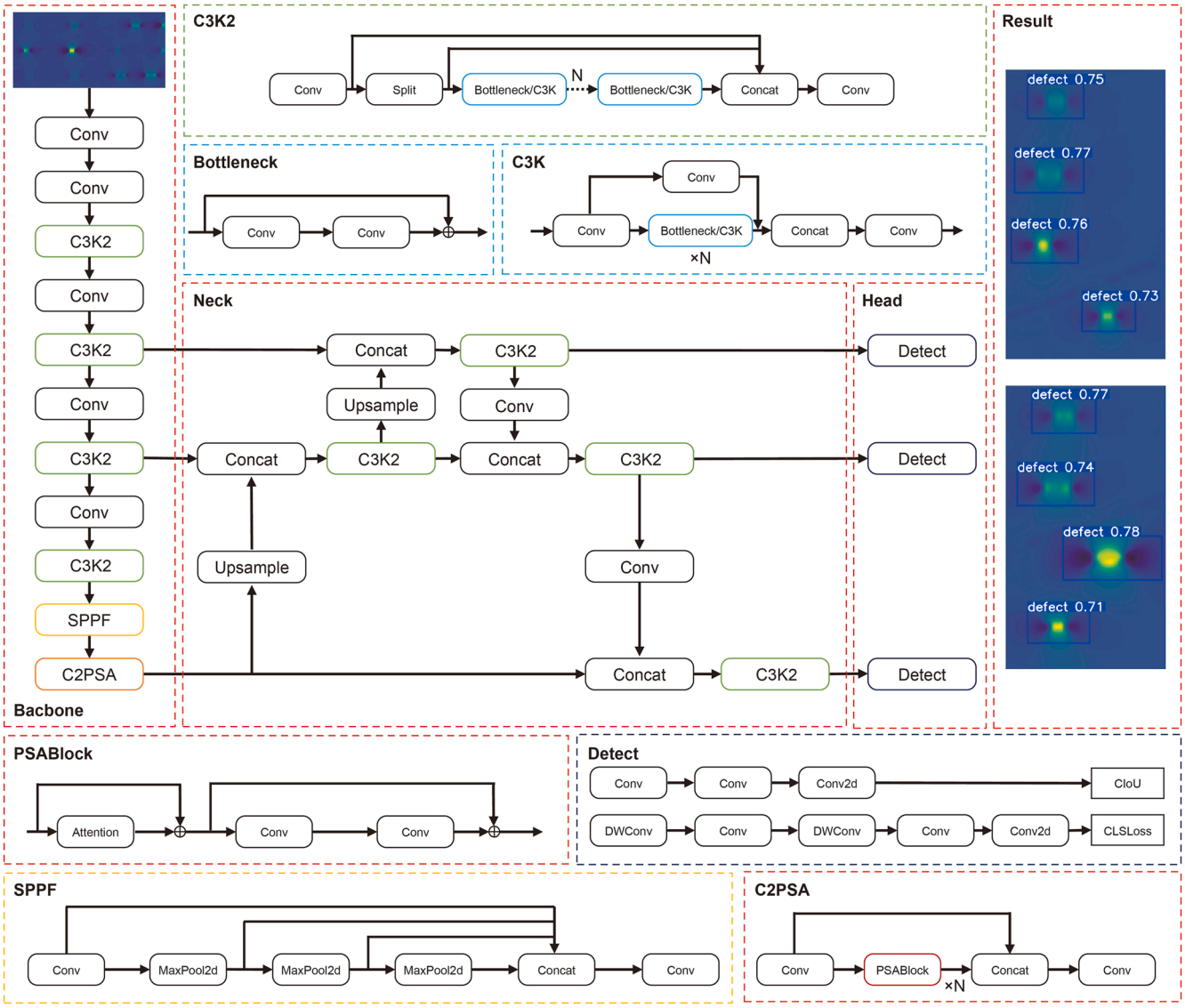

Fig. 8. The YOLOv11 model structure.

Table 1
Physical information features.

Feature	Calculation equation	Feature	Calculation equation
f_1	$\max(H_x) - \min(H_x)$	f_4	$\int_{\mathrm{argmin}(H_y')}^{\mathrm{argmax}(H_y')} H_y$
f_2	$\mathrm{argmax}(H_y') - \mathrm{argmin}(H_y')$	f_5	$\int_{\mathrm{argmin}(H_y')}^{\mathrm{argmax}(H_y')} (H_y)^2$
f_3	$\max(H_y) - \min(H_y)$	f_6	$\max(H_z) - \min(H_z)$

Table 2
The CNN model's structural parameters.

Stage	Structure
Stage 1	8 Conv2d 3 × 2 + BatchNormal2d + Relu +
	16 Conv2d 3 × 2 + BatchNormal2d + Relu +
Stage 2	32 Conv2d 3 × 2 + BatchNormal2d + Relu +
	64 Conv2d 3 × 2 + BatchNormal2d + Relu + Maxpool2d
Stage 3	64 Conv2d 3 × 2 + BatchNormal2d + Relu +
	128 Conv2d 3 × 2 + BatchNormal2d + Relu + Maxpool2d
Stage 4	Linear

dimensions predicted by the network are integrated with the physical information features during the loss function construction. Namely, by jointly optimizing the geometric parameter error term and the physical feature consistency constraint, the proposed model ensures that, during the learning process of defect dimensions, the predicted results remain within a physically reasonable range, thus improving the model's robustness and practical applicability. The loss function is defined as follows:

$$\mathrm{Loss}_{\mathrm{total}} = \lambda_{\mathrm{obj}} \sum_{i=\mathrm{length,width,depth}} \mathrm{Loss}\left(i_{\mathrm{predicted}}, i_{\mathrm{true}}\right) + \lambda_{\mathrm{physics}} \sum_{i=1}^{6} \mathrm{Loss}\left(f_{i_{\mathrm{true}}}, f_{i_{\mathrm{predicted}}}\right), \quad (6)$$

where λ_{obj} is the loss weight between the defect geometric parameters (length, width, and depth) predicted by the model and their true values; $\lambda_{\mathrm{physics}}$ is the loss weight between the physical information feature set $[f_1, f_2, f_3, f_4, f_5, f_6]$ predicted by the model and the true feature values. In this study, both $\lambda_{\mathrm{physics}}$ and λ_{obj} are set to 0.5 to achieve a balanced optimization between the model's fitting loss of defect geometrical parameters and the loss of extracting physical features. To improve optimization efficiency, this study selects the mean squared error (MSE) as a supervision function. Its convexity property accelerates the convergence of the gradient descent algorithm and prevents it from falling into local extrema. Further, the continuous differentiability ensures the stability of backpropagation, and the squared operation amplifies significant errors, making the model prioritize correcting the key parameters' deviations. To improve the model's training effect and reduce training time, the study uses a deep-learning model pre-trained on the COCO dataset. The model structure is shown in Fig. 9.

3.3. Cascaded defect detection and size estimation model design

The cascaded MFL-data deep-learning processing workflow constructed in this study is presented in Fig. 10. The proposed method includes three stages. In the first stage, a pipeline intelligent inspection robot collects MFL data on pipeline defects. Then, experts perform baseline calibration and noise reduction on the collected MFL signal data and transform the *y*-axis MFL data into a spectral representation, converting the MFL data into pseudo-color images. The defect's relative center coordinates, length, and width in the pseudo-color image are extracted, and several defect sample location labels are established. Next, the YOLOv11 model is trained on the constructed labeled dataset to construct a defect location recognition model. For the defect size estimation model, the three-axis MFL ILI data are extracted along with partial defect size information (i.e., the length, width, and depth of a defect) to construct a small defect size sample database. Using this database, the proposed physics-informed and data-driven prior deep-learning model for defect size estimation is trained, ultimately obtaining the size information on defects at different locations to provide data support for subsequent integrity evaluation.

4. Results and discussions

This section provides a detailed presentation of the training and testing results of the proposed cascaded deep-learning model for defect detection and size estimation. Following the structure displayed in Fig. 10, the MFL ILI data processing workflow used the preprocessed MFL data as a foundation. The pre-trained YOLOv11 model and the physics-informed and data-driven prior deep-learning model operated in an offline data analysis mode to obtain information on the defect's location and size.

4.1. Experimental conditions and model evaluation metrics

To ensure the fairness of experiments, all tests in this study were conducted on the same experimental platform. The hardware setup included one AMD Ryzen 9 7845HX@3.0 GHz 12-core 24-thread processor, a GeForce RTX 4070 Laptop GPU, and 32 GB of RAM. The operating system was Windows 11, and the model framework was based on PyTorch 2.0.1 with CUDA version 11.8.

To evaluate the effectiveness of defect detection and quantification, this study selected seven common evaluation metrics: precision, recall, F1-score, AP50, goodness of fit (Gof), mean absolute percentage error (MAPE), and mean absolute error (MAE). The calculation equations of the precision, recall, and F1-score were defined as follows:

$$\mathrm{Precision} = \frac{TP}{TP + FP} \times 100\%, \quad (7)$$

$$\mathrm{Recall} = \frac{TP}{TP + FN} \times 100\%, \quad (8)$$

$$\mathrm{F1\text{-}score} = \frac{2 \times \mathrm{precision} \times \mathrm{recall}}{\mathrm{precision} + \mathrm{recall}} \times 100\%, \quad (9)$$

where *TP* (true positive) is the number of correctly predicted defect samples; *FP* (false positive) is the number of background areas incorrectly predicted as defects; *FN* (false negative) is the number of defects incorrectly predicted as background; *TN* (true negative) is the number of background samples correctly predicted as background.

The AP50 metric was calculated by:

$$\mathrm{AP50} = \int \mathrm{precision}(\mathrm{recall})\mathrm{drecall}, \quad (10)$$

where AP50 refers to the average precision when the intersection over union (IoU) threshold was set to 0.5, meaning that a predicted bounding box was considered a true positive only if its IoU with the GT bounding box was greater than 0.5.

The Gof, MAPE, and MAE values were respectively obtained by:

$$\mathrm{Gof} = \frac{SSR}{SST} = 1 - \frac{SSE}{SST} = 1 - \frac{\sum_{i=1}^{n}(y_i - \hat{y}_i)^2}{\sum_{i=1}^{n}(y_i - \bar{y})^2}, \quad (11)$$

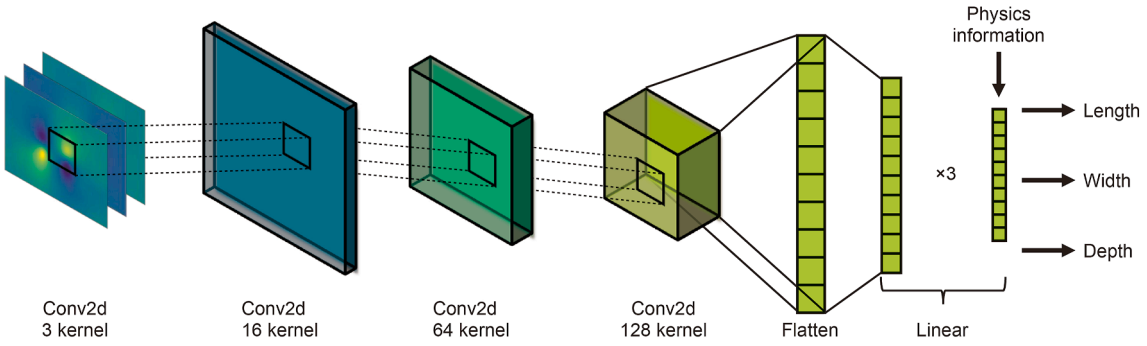

Fig. 9. The structure of the physics-informed and data-driven prior deep-learning model.

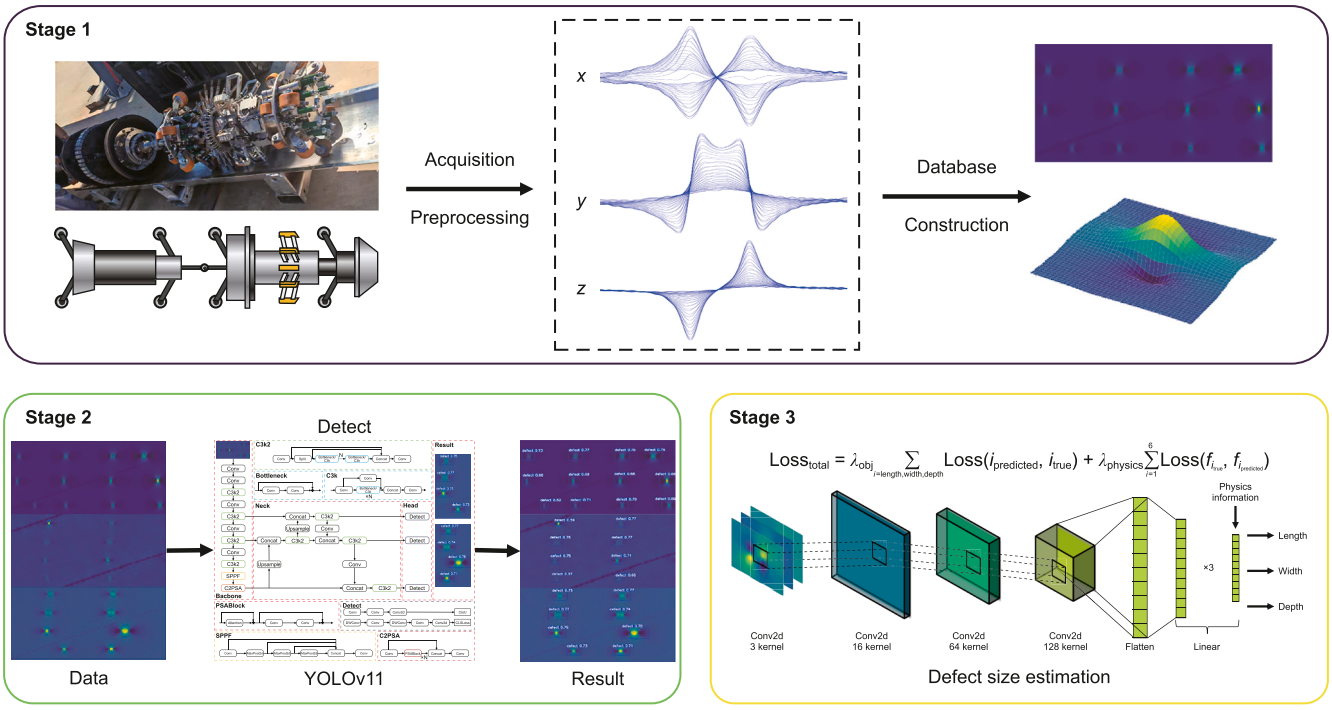

Fig. 10. The cascaded defect detection and size estimation model.

$$\mathrm{MAPE} = \frac{1}{n}\sum_{i=1}^{n}\frac{|y_i - \hat{y}_i|}{y_i} \times 100\%, \tag{12}$$

$$\mathrm{MAE} = \frac{1}{n}\sum_{i=1}^{n}|y_i - \hat{y}_i|, \tag{13}$$

where n is the number of predicted samples; y_i and $\hat{y}_i$ represent the true and predicted values of the defect size, respectively; $\bar{y}$ is the mean value of the GT defect size labels.

4.2. Detection model effectiveness validation and different model comparison

To validate the model's performance, the constructed dataset was divided into training, testing, and validation sets according to the ratio of 8:1:1. The batch size for training was set to 32, the learning rate was 0.01, and the maximum number of iterations was set to 100. The model was configured to save the best-performing parameters during training. The loss curves during the training process of the YOLOv11 model, including the classification loss, bounding box regression loss, and distribution focal loss for both the training and testing sets, as well as the curves of precision, recall, and F1-score, are presented in Fig. 11.

The detection results of the YOLOv11 model are presented in Fig. 12. The results indicated that the YOLOv11 model, trained on the established defect detection dataset, could effectively detect pipeline defects. For the confidence threshold and IoU threshold of 0.6 on the test set, the standard YOLOv11 model achieved 100% precision, an 84.29% recall, a 91.47% F1-score, and a 92.14% AP50 in binary defect detection. These values demonstrated that the trained YOLOv11 model could accurately detect and locate pipeline defects.

To validate the superiority of the proposed YOLOv11 model, this study compared it with the YOLOv8 and YOLOv5 models (Chen et al., 2024; Yuksel et al., 2023). Table 3 presents the comparison results of the prediction performance and operational efficiency of different models on the same test set. The results indicated that compared to the other methods, the proposed YOLOv11 model had higher detection accuracy, with an AP50 value reaching 92.14%. Particularly, compared to the YOLOv8 and YOLOv5 models, the AP50 value of the proposed model increased by 1.02% and 1.71%, respectively. To reduce deployment difficulties caused by hardware limitations, this study also compared the floating-point operations (GFLOPs) and inference speed per image of different models. The proposed YOLOv11 model required only 6.3 GFLOPs, with an image inference speed as high as 5.6 ms. A comprehensive comparison showed that the proposed model had the smallest computational load, the fastest inference speed, and the highest prediction accuracy among all the models.

4.3. Size estimation effectiveness verification and ablation experiments

A properly selected training method and appropriate hyperparameter settings denote key factors in ensuring the effectiveness of model training. The study divides the dataset into a training set and a test set according to a 9:1 ratio. The Adam optimizer was used, and an initial learning rate was set to 5×10^{-3}. The Adam optimizer was selected in this study because, compared to the traditional SGD optimizer, it has faster convergence and stronger robustness (Fig. 13(a)). In addition, a learning rate decay strategy was applied during the training process, and the learning rate decreased stepwise with the number of training epochs, as shown in Table 4. The learning rate decay strategy helped the model approach the local or global optimal solution continuously and ensured that the model's loss did not fluctuate significantly in the later stages. As shown in Fig. 13, it can be seen that when the number of training epochs reaches 600, both the training loss and testing loss have basically converged, and the training time is only 59 s. Considering both training stability and efficiency, the number of training epochs is finally set to 600.

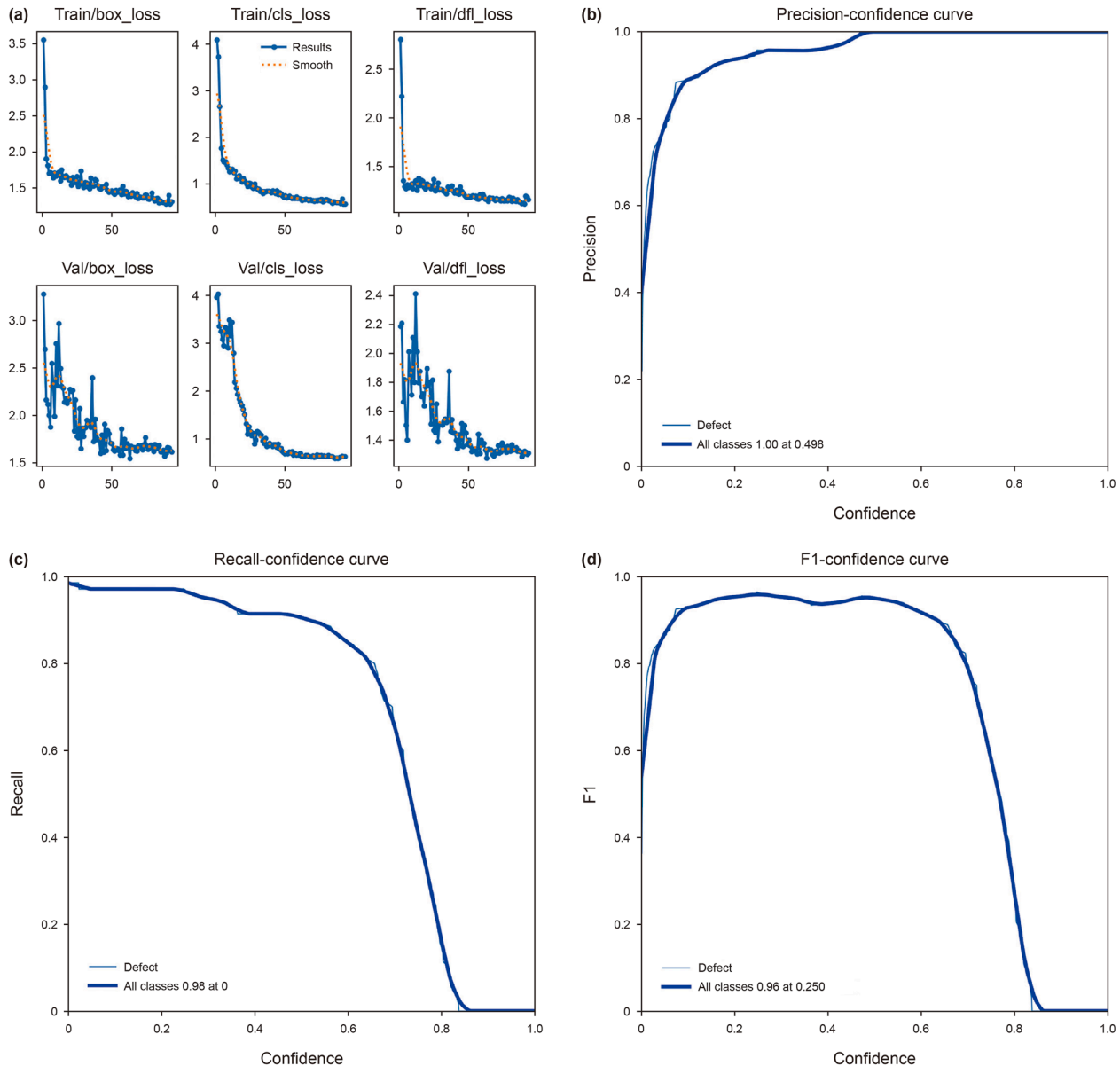

Fig. 11. The YOLOv11 model training parameters and test results: (**a**) loss curve; (**b**) precision curve; (**c**) recall curve; (**d**) F1-score curve.

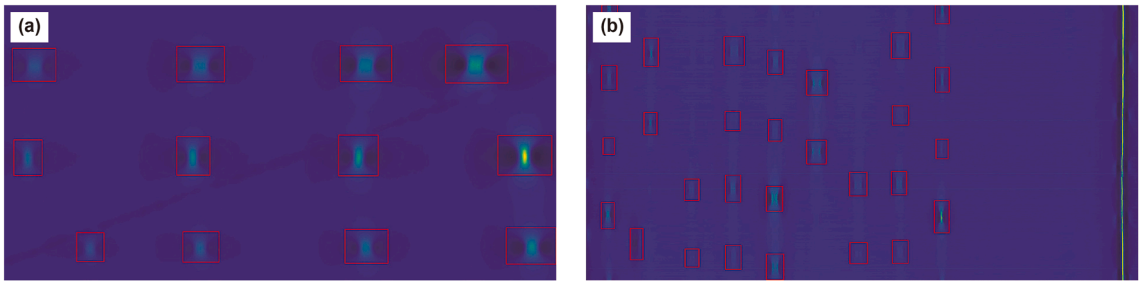

Fig. 12. The defect detection results of the YOLOv11 model: (**a**) case 1; (**b**) case 2.

To validate the effectiveness of the proposed method, this study tested it on the test set, as shown in Table 5. Through calculations and validation, the physics-informed and data-driven prior deep-learning model achieved the Gof and MAPE values of 99.06% and 5.13% for defect length, 98.51% and 11.52% for defect width, and 94.8% and 6.29% for defect depth, respectively. This indicated that the proposed model could effectively predict the three-dimensional dimensions of defects.

Table 3
The effectiveness and operational efficiency comparison of different models.

Model	Evaluation metric					
	AP50	Precision	Recall	F1-score	GFLOPs	Inference time, ms
YOLOv11	92.14	100	84.29	91.47	6.3	5.6
YOLOv8	91.12	100	82.86	90.62	8.1	16.1
YOLOv5	90.43	98.28	81.43	89.06	7.1	21.2

Further, to validate the superiority of the proposed defect size estimation model, this study made predictions using the pure data-driven CNN model and the TabPFN model (Hollmann et al., 2025) on the same dataset. The corresponding physical information features are also incorporated as inputs into the TabPFN model to fit the three-dimensional dimensions of the defects. The prediction results are presented in Table 6 and Fig. 14.

The fitting results show that the TabPFN model performs well in predicting defect length under small-sample conditions, achieving a Gof of 99.92% and a MAPE of only 3.27%. However, its performance in predicting defect width and depth is significantly weaker, with a Gof of only 69.02% and a MAPE of 30.60% for width, and a Gof of 83.73% and a MAPE of 16.40% for depth. These results indicate that although TabPFN has strong capabilities in modeling tabular data, its ability to capture complex geometric features such as defect width and depth is limited when relying solely on manually extracted features. Therefore, it is necessary to directly use defect samples as model inputs and leverage the powerful nonlinear feature extraction capability of CNN to automatically learn and model key defect characteristics.

Compared to the pure data-driven CNN model, the proposed deep-learning model achieved better fitting performance, with the MAPE value reduced by 6.9%, 10.19%, and 4.9% for the defect length, width, and depth, respectively. Thus, by incorporating physical information supervision, the model's fitting performance was effectively improved.

As depicted in Fig. 15, compared to the other models, the proposed model had a lower MAE, and its errors were more

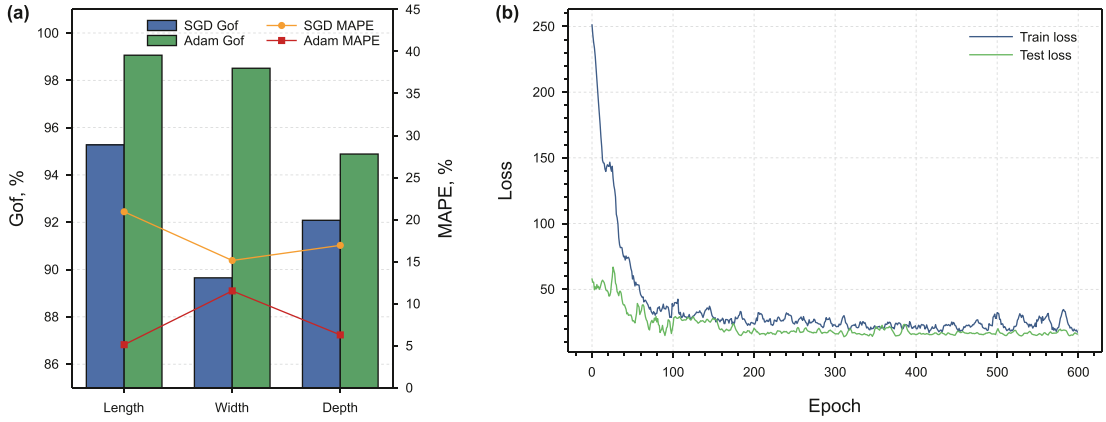

Fig. 13. Model parameter analysis: (**a**) experiment results with different optimizer; (**b**) loss value with different epochs.

Table 4
Learn rate decay.

Epoch number	Learning rate
$0 \leq$ Epoch ≤ 150	5×10^{-3}
$150 <$ Epoch ≤ 300	1×10^{-3}
$300 <$ Epoch ≤ 400	1×10^{-5}
$400 <$ Epoch ≤ 600	1×10^{-6}

Table 6
Comparison results and ablation experiments.

Model	Metric					
	Length		Width		Depth	
	Gof, %	MAPE, %	Gof, %	MAPE, %	Gof, %	MAPE, %
Physics + data	99.06	5.13	98.51	11.52	94.8	6.29
Data	96.88	12.03	89.04	21.71	93.65	11.19
TabPFN	99.92	3.27	69.02	30.60	83.73	16.40

Table 5
Model prediction results.

True length, mm	True width, mm	True depth, %	Predicted length, mm	Predicted width, mm	Predicted depth, %
20.0	70.0	40.0	19.3	70.2	38.4
15.0	40.0	40.0	13.8	42.2	38.9
60.0	25.0	40.0	57.7	22.9	38.9
40.0	15.0	80.0	47.6	13.9	70.1
15.0	80.0	60.0	15.7	79.1	59.3
90.0	10.0	60.0	94.2	14.3	46.5
25.0	60.0	20.0	24.7	63.5	19.1
100.0	20.0	20.0	92.3	15.5	23.4
90.0	10.0	80.0	87.3	11.4	79.7
20.0	100.0	30.0	20.2	95.5	29.6
100.0	20.0	80.0	101.6	19.5	79.3
20.0	90.0	20.0	20.5	84.7	19.4
10.0	30.0	30.0	9.3	38.6	29.9
100.0	20.0	40.0	95.6	17.8	33.9

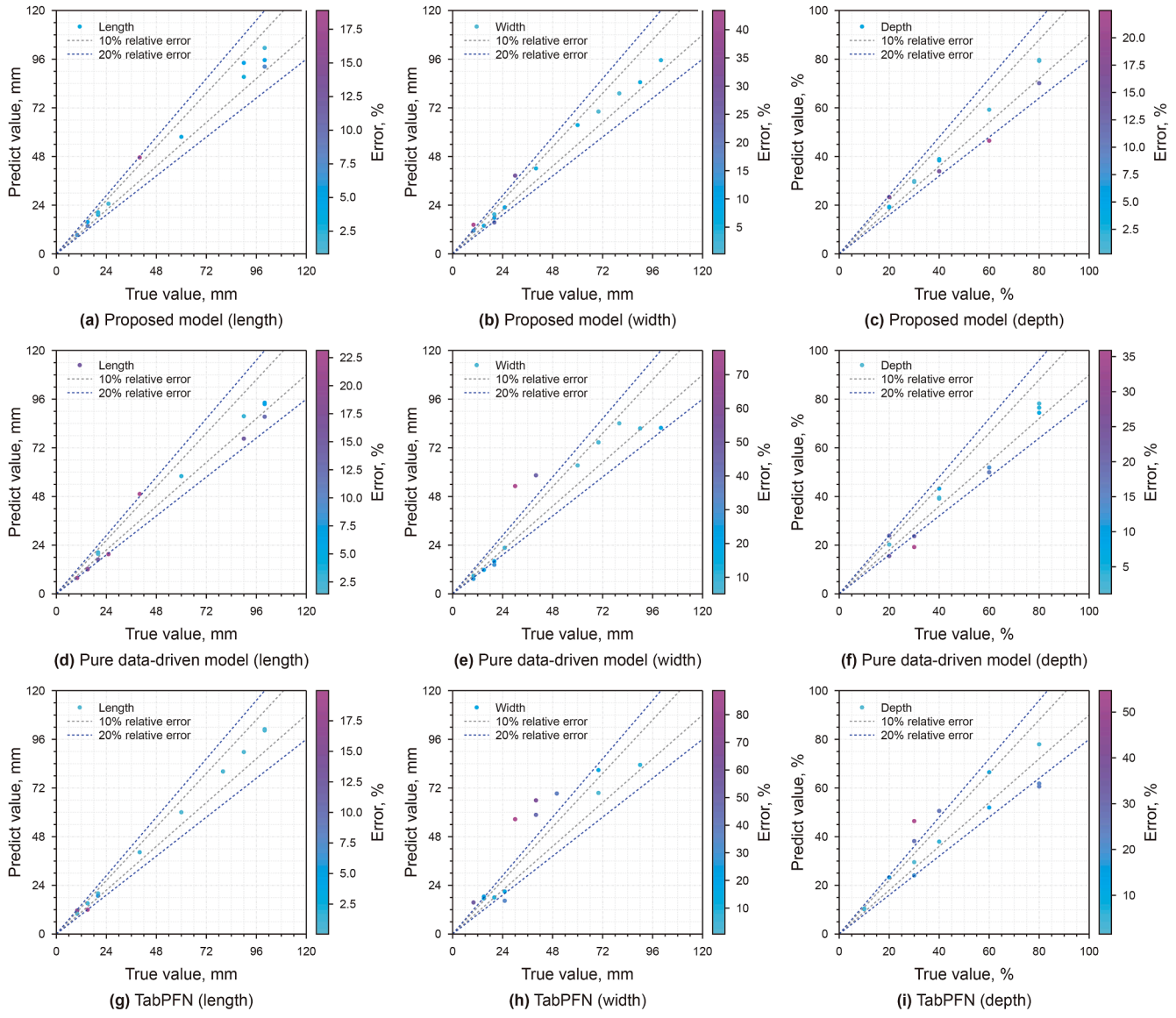

Fig. 14. Fitting results comparison of different models.

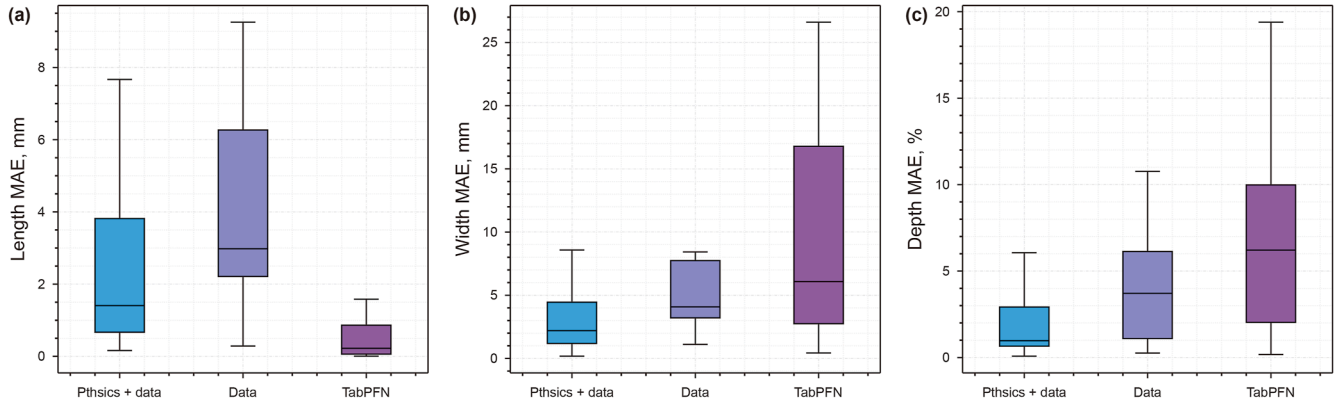

Fig. 15. Defect size quantification results of the experiment in terms of the MAE metric: (**a**) length; (**b**) width; (**c**) depth.

concentrated in the lower error region. This indicated that, compared to the TabPFN and pure data-driven models, the proposed method could provide higher precision and greater robustness. This was because the proposed method integrated defect size quantification theory and defect size labels, which jointly guided and corrected the network fitting effect. In practical pipeline MFL data applications, the proposed method could improve poor model fitting results caused by the lack of data, thus enhancing the model's generalization ability.

5. Conclusion

This study conducts the MFL ILI pulling through testing to perform noise reduction on the MFL data, constructs a pipeline defect detection database and a defect size estimation database, and applies the pre-trained YOLOv11 algorithm and a physics-informed and data-driven prior deep-learning model algorithm to construct a cascaded pipeline defect location and quantification algorithm.

The main conclusions of this study can be summarized as follows.

(1) An ILI platform is established at the Beijing Daxing pulling through the testing site, using an ultra-high-definition MFL (240-channel) ILI intelligent robot to inspect a 508-mm diameter pipeline, where 134 artificial defects are manually created;
(2) The baseline calibration and two-dimensional Gaussian filtering are performed to denoise the MFL ILI data. The denoised y-axis MFL data are mapped to the [0, 255] range, generating a pseudo-color image of the y-axis MFL data, and defect locations are marked to establish a defect detection database. The three-axis MFL data are extracted according to the pipeline defect blueprint to construct a defect quantification database;
(3) The pre-trained YOLOv11 model is developed to identify defect locations. Compared to the YOLOv8 and YOLOv5 models, the AP50 of the proposed model is improved by 1.02% and 1.71%, respectively, thus effectively enhancing defect recognition performance;
(4) An in-depth analysis of the MFL data characteristics is conducted, and six representative physical features are selected to construct a physics-informed and data-driven prior deep-learning model for defect size quantification. The designed model achieves the Gof and MAPE values of 99.06% and 5.127% for defect length, 98.51% and 11.52% for defect width, and 94.88% and 6.29% for defect depth, respectively.

Future work could further analyze the real operational pipeline MFL inspection data to establish a practical MFL defect detection and quantification database and develop lightweight and accurate models for defect identification and quantification.

CRediT authorship contribution statement

Xi-Ming Chen: Writing – review & editing, Writing – original draft, Methodology, Data curation. **Meng-Kai Fu:** Writing – review & editing, Methodology, Data curation. **Jia Shao:** Validation, Investigation. **Xiao-Ben Liu:** Funding acquisition, Conceptualization.

Declaration of competing interest

Authors declare that they have no known competing financial interests or personal relationships that could have appeared to influence the work reported in this paper.

Acknowledgments

This research has been co-financed by Key Science and Technology Project of Ministry of Emergency Management of the People's Republic of China (Grant No. 2024EMST090903), National Key R&D Program of China (Grant No. 2022YFC3070100), and Young Elite Scientists Sponsorship Program by Beijing Association for Science and Technology (Grant No. BYESS2023261).

References

Ahmed, F., Ali, L., Iqbal, J., et al., 2008. Failure of pipe joints during hydrostatic testing. Eng. Fail. Anal. 15, 766–773. https://doi.org/10.1016/j.engfailanal.2007.06.008.
Akdoğan, C., Özer, T., Oğuz, Y., 2025. PP-YOLO: deep learning based detection model to detect Apple and cherry trees in orchard based on histogram and wavelet preprocessing techniques. Comput. Electron. Agric. 232, 110052. https://doi.org/10.1016/j.compag.2025.110052.
Chen, P.C., Li, R., Fu, K., et al., 2021. Research and method for in-line inspection technology of girth weld in long-distance oil and gas pipeline. J. Phys. Conf. 1986, 012052. https://doi.org/10.1088/1742-6596/1986/1/012052.
Chen, P.C., Li, R., Fu, K., et al., 2024. A cascaded deep learning approach for detecting pipeline defects via pretrained YOLOv5 and ViT models based on MFL data. Mech. Syst. Signal Process. 206, 110919. https://doi.org/10.1016/j.ymssp.2023.110919.
Cole, I.S., Marney, D., 2012. The science of pipe corrosion: a review of the literature on the corrosion of ferrous metals in soils. Corros. Sci. 56, 5–16. https://doi.org/10.1016/j.corsci.2011.12.001.
Deif, S., Daneshmand, M., 2019. Multiresonant chipless RFID array system for coating defect detection and corrosion prediction. IEEE Trans. Ind. Electron. 67 (10), 8868–8877. https://doi.org/10.1109/TIE.2019.2949520.
Feng, Q.S., Zhang, H.L., Wang, C.M., et al., 2016. Advantages of three-axial high-resolution magnetic flux leakage inspection technology and its application status. Oil Gas Storage Transp. 35 (10), 5. https://doi.org/10.6047/j.issn.1000-8241.2016.10.004 (in Chinese).
Gao, B., Bai, L.B., Woo, W.L., et al., 2014. Automatic defect identification of eddy-current pulsed thermography using single channel blind source separation. IEEE Trans. Instrum. Meas. 63, 913–922. https://doi.org/10.1109/TIM.2013.2285789.
Guo, L., Ding, J.Q., Li, Z.W., et al., 2024. Magnetic flux leakage defect recognition method based on attention feature fusion. Journal of Shenyang University of Technology 46 (2), 212–218. https://doi.org/10.7688/j.issn.1000-1646.2024.02.15 (in Chinese).
Han, F.C., Lang, X.M., 2023. A fast magnetic flux leakage small defect detection network. IEEE Trans. Ind. Inf. 19 (12), 11941–11948. https://doi.org/10.1109/TII.2023.3280950.
Hollmann, N., Müller, S., Purucker, L., et al., 2025. Accurate predictions on small data with a tabular foundation model. Nature 637 (8045), 319–326. https://doi.org/10.1038/s41586-024-08328-6.
Howard, A.G., Zhu, M., Chen, B., et al., 2017. Mobilenets: efficient convolutional neural networks for mobile vision applications. arXiv preprint arXiv: 170404861. https://doi.org/10.48550/arXiv.1704.04861.
Jiang, L., Zhang, H.G., Liu, J.H., et al., 2022. THMS-Net: a two-stage heterogeneous signals mutual supervision network for MFL weak defect detection. IEEE Trans. Instrum. Meas. 71, 1–9. https://doi.org/10.1109/TIM.2022.3198762.
Khodayari-Rostamabad, A., Reilly, J.P., Nikolova, N.K., et al., 2009. Machine learning techniques for the analysis of magnetic flux leakage images in pipeline inspection. IEEE Trans. Magn. 45 (8), 3073–3084. https://doi.org/10.1109/TMAG.2009.2020160.
Kim, H.M., Yoo, H.R., Park, G.S., 2018. A new design of MFL Sesnsors for self-driving NDT robot to avoid getting stuck in curved underground pipelines. IEEE Trans. Magn. 54, 1–5. https://doi.org/10.1109/TMAG.2018.2846283.
Liu, B., He, L., Zhang, H., et al., 2017. The axial crack testing model for long distance oil-gas pipeline based on magnetic flux leakage internal inspection method. Measurement 103, 275–282. https://doi.org/10.1016/j.measurement.2017.02.051.
Liu, B., Luo, N., Feng, G., 2021. Quantitative study on MFL signal of pipeline composite defect based on improved magnetic charge model. Sensors 21 (10), 3412. https://doi.org/10.3390/s21103412.
Liu, J.H., Fu, M.R., Tang, J.H., 2016. MFL inner detection based defect recognition method. Chin. J. Sci. Instrum. 37 (11), 2572–2581. https://doi.org/10.3969/j.issn.0254-3087.2016.11.021 (in Chinese).
Liu, J.H., Wen, Z.T., Shen, X.K., et al., 2024. Online pipeline weld defect detection for magnetic flux leakage inspection system via lightweight rotated network. IEEE Trans. Ind. Electron. 72 (7), 7573–7584. https://doi.org/10.1109/TIE.2024.3503635.
Liu, X.B., Liu, S., Ji, B.L., et al., 2021. Intelligent identification method of pipeline sections with bending deformation based on IMU data. Oil Gas Storage Transp. 40 (11), 1228–1235. https://doi.org/10.6047/j.issn.1000-8241.2021.11.004 (in Chinese).

Liu, Y.M., Bao, Y., 2022. Review on automated condition assessment of pipelines with machine learning. Adv Eng Informatics 53, 101687. https://doi.org/10.1016/j.aei.2022.101687.
Long, Y., Huang, S., Peng, L., et al., 2021. A characteristic approximation approach to defect opening profile recognition in magnetic flux leakage detection. IEEE Trans. Instrum. Meas. 70, 1–12. https://doi.org/10.1109/TIM.2021.3050185.
Long, Y., Zhang, J.H., Huang, S.L., et al., 2022. A novel crack quantification method for ultra-high-definition magnetic flux leakage detection in pipeline inspection. IEEE Sens. J. 22 (16), 16402–16413. https://doi.org/10.1109/JSEN.2022.3190684.
Melo, C., Dann, M.R., Hugo, R.J., et al., 2020. Optimal locations for non-destructive inspections to verify direct assessment of internally corroded pipelines. Upstream Oil and Gas Technology 5, 100008. https://doi.org/10.1016/j.upstre.2020.100008.
Miller, S., Sander, F., 2006. Advances in feature identification using tri-axial MFL sensor technology. In: Proceedings of Proceedings of the 2006 International Pipeline Conference. Calgary, Alberta, Canada.
Nepal, U., Eslamiat, H., 2022. Comparing YOLOv3, YOLOv4 and YOLOv5 for autonomous landing spot detection in faulty UAVs. Sensors 22 (2), 464. https://doi.org/10.3390/s22020464.
Parlak, B.O., Yavasoglu, H.A., 2023. A comprehensive analysis of in-Line inspection tools and technologies for steel oil and gas pipelines. Sustainability 15 (3), 2783. https://doi.org/10.3390/su15032783.
Peng, X., Anyaoha, U., Liu, Z., et al., 2020. Analysis of magnetic-flux leakage (MFL) data for pipeline corrosion assessment. IEEE Trans. Magn. 56, 1–15. https://doi.org/10.1109/TMAG.2020.2981450.
Reber, K., Beller, M., Willems, H.H., et al., 2002. A new generation of ultrasonic in-line inspection tools for detecting, sizing and locating metal loss and cracks in transmission pipelines. In: Proceedings of 2002 IEEE Ultrasonics Symposium. Munich, Germany.
Redmon, J., Divvala, S., Girshick, R., et al., 2016. You only look once: unified, real-time object detection. In: Proceedings of Proceedings of the IEEE Conference on Computer Vision and Pattern Recognition. Las Vegas, NV, USA.
Ren, Y.F., Liu, J.H., Zhao, H., et al., 2024. An industrial fault sample reconstruction and generation method under limited samples with missing information. IEEE Transactions on Systems, Man, and Cybernetics: Systems 54 (12), 7821–7833. https://doi.org/10.1109/TSMC.2024.3459633.
Shen, X.K., Liu, J.H., Jiang, L., et al., 2023. A novel weld defect detection method for intelligent magnetic flux leakage detection system via contextual relation network. IEEE Trans. Ind. Electron. 71 (6), 6304–6314. https://doi.org/10.1109/TIE.2023.3294578.
Shen, X.K., Liu, J.H., Ren, Y.F., et al., 2025. A task-oriented physical collaborative network for pipeline defect diagnosis in a magnetic flux leakage detection system. Comput. Ind. 169, 104290. https://doi.org/10.1016/j.compind.2025.104290.
Sun, H.Y., Peng, L.S., Huang, S.L., et al., 2021. Development of a physics-informed doubly fed cross-residual deep neural network for high-precision magnetic flux leakage defect size estimation. IEEE Trans. Ind. Inf. 18 (3), 1629–1640. https://doi.org/10.1109/TII.2021.3089333.
Wang, C.Y., Liao, H.Y.M., Wu, Y.H., et al., 2020. CSPNet: a new backbone that can enhance learning capability of CNN. In: Proceedings of the IEEE/CVF Conference on Computer Vision and Pattern Recognition Workshops. Seattle, WA, USA.
Wang, L., Ma, L.J., Xu, J., et al., 2023. Deformed section identification of oil and gas pipeline based on deep learning. China Petroleum Machinery 51 (11), 11–19. https://doi.org/10.16082/j.cnki.issn.1001-4578.2023.11.002 (in Chinese).
Wang, L., Zhang, H.G., Liu, J.H., et al., 2022. Defect size quantification for pipeline magnetic flux leakage detection system via multilevel knowledge-guided neural network. IEEE Trans. Ind. Electron. 70 (9), 9550–9560. https://doi.org/10.1109/TIE.2022.3210557.
Wang, L., Zhang, H.G., Liu, J.H., et al., 2024. Irregular defect size estimation for the magnetic flux leakage detection system via expertise-informed collaborative network. IEEE Trans. Ind. Electron. 71 (10), 13189–13200. https://doi.org/10.1109/TIE.2024.3357845.
Wang, L., Zhang, H.G., Liu, J.H., et al., 2025. A mechanism-aided bilevel knowledge transfer framework for pipeline corrosion condition quantitative assessment. IEEE Trans. Ind. Inf. https://doi.org/10.1109/TII.2025.3574535.
Xie, M.J., Tian, Z.G., 2018. A review on pipeline integrity management utilizing in-line inspection data. Eng. Fail. Anal. 92, 222–239. https://doi.org/10.1016/j.engfailanal.2018.05.010.
Xu, L.S., Dong, S.H., Chen, S.Y., et al., 2024. Research on quantification of magnetic flux leakage signals of pipeline defect based on AOA-XGBOOST model. Journal od Science and Technology 20 (12), 75–81. https://doi.org/10.11731/j.issn.1673-193x.2024.12.010 (in Chinese).
Yang, J.W., 2005. High precision pipeline magnetic flux leakage on-line inspection technology. Journal of Shenyang University of Technology 27 (5), 522–525. https://doi.org/10.3969/j.issn.1000-1646.2005.05.012 (in Chinese).
Yu, J., Tang, J.H., Shen, X.K., et al., 2023. Intelligent detection method for submarine pipelines based on faster R-CNN. China Saf. Sci. J. 33 (6), 80. https://doi.org/10.16265/j.cnki.issn1003-3033.2023.06.2360 (in Chinese).
Yuan, J., Qiao, M.T., Hu, C., et al., 2024. A classification and quantitative assessment method for internal and external surface defects in pipelines based on ASTC-net. Adv. Eng. Inform. 61, 102492. https://doi.org/10.1016/j.aei.2024.102492.
Yuksel, V., Tetik, Y.E., Basturk, M.O., et al., 2023. A novel cascaded deep learning model for the detection and quantification of defects in pipelines via magnetic flux leakage signals. IEEE Trans. Instrum. Meas. 72, 1–9. https://doi.org/10.1109/TIM.2023.3272377.
Zarifi, M.H., Deif, S., Abdolrazzaghi, M., et al., 2018. A microwave ring resonator sensor for early detection of breaches in pipeline coatings. IEEE Trans. Ind. Electron. 65, 1626–1635. https://doi.org/10.1109/TIE.2017.2733449.
Zhang, D., Liu, X.B., Fu, M.K., et al., 2025. A novel local deformation pipe section identification method via IMU detection data and hybrid deep learning model. Mech. Syst. Signal Process. 224, 112091. https://doi.org/10.1016/j.ymssp.2024.112091.
Zhang, H., Zu, K.K., Lu, J., et al., 2022. EPSANet: an efficient pyramid squeeze attention block on convolutional neural network. In: Proceedings of the Asian Conference on Computer Vision. Macao, China.
Zhang, M., Guo, Y.B., Xie, Q.J., et al., 2022. Estimation of defect size and cross-sectional profile for the oil and gas pipeline using visual deep transfer learning neural network. IEEE Trans. Instrum. Meas. 72, 1–13. https://doi.org/10.1109/TIM.2022.322505.
Zhang, P., Gao, W.Z., Li, Y., et al., 2021. Misfire detection of diesel engine based on convolutional neural networks. Proc. Inst. Mech. Eng. - Part D J. Automob. Eng. 235 (8), 2148–2165. https://doi.org/10.1177/0954407020987077.
Zhang, S.Z., Li, H.M., Zhao, C.T., 2023. Defect-depth-field algorithm for simulating magnetic flux leakage signals based on discrete magnetic dipole model. NDT E Int. 139, 102939. https://doi.org/10.1016/j.ndteint.2023.102939.
Zhang, Z., Tanimoto, Y., Iwata, M., et al., 2025. Data generation using Pix2Pix to improve YOLO v8 performance in UAV-based Yuzu detection. Smart Agricultural Technology 10, 100777. https://doi.org/10.1016/j.atech.2025.100777.
Zhao, H., Liu, J.H., Zhang, H.G., et al., 2024. A masked multi-view bidirectional network for class extremely imbalanced object detection under magnetic flux leakage signals. IEEE Trans. Autom. Sci. Eng. 22, 905–915. https://doi.org/10.1109/TASE.2024.3355984.
Zhao, S.X., Tian, Y., 2024. Identification and size quantification of pipeline corrosion defects based on PP-YOLOE and MTL. Oil & Gas Storage and Transportation 43 (12), 1355–1364. https://doi.org/10.6047/j.issn.1000-8241.2024.12.004 (in Chinese).
Zhao, Z.H., Jie, G., Wen, J., 2021. A time series classification method based on 1DCNN-FNN. In: Proceedings of 2021 33rd Chinese Control and Decision Conference (CCDC). Kunming, China.